Transport of porous particles in channel flow

Bernat Font

31/01/2021

The transport of particles in micro-channels has multiple engineering and biomedical applications. In physiological flows, cells advected by bloodstream experience shear and normal stresses causing cell deformation and displacement. In this work, Darcy flow will be used to model porous particles, or cells, immersed in a low-Reynolds planar micro-channel. In particular, we will focus in the dynamics of multiple particles, governed by Darcy's law, advected by channel flow, governed by the incompressible Navier–Stokes equations. The problem set-up is visualised in Fig. 1. Particles can be represented by a patch of Darcy flow or by a Darcy flow region surrounding a solid body. In the initial stage, the former representation is chosen.

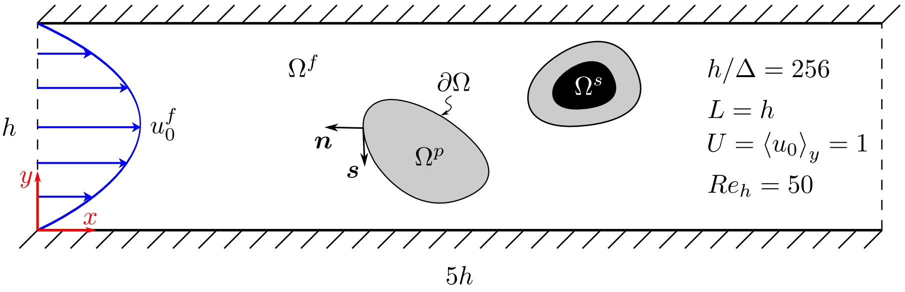

Figure 1: Problem description. Ω^f is the Navier-Stokes fluid domain. Ω_p is the porous particle domain modelled with Darcy flow. Ω_s is the solid domain. $\partial\Omega$ is the interface between Ω^f and Ω^p. $\boldsymbol{n}$ and $\boldsymbol{s}$ the normal and tangential vectors to the porous surface, respectively. h is the channel height. Δ is the grid spacing. L and U are the characteristic length and velocity, respectively.

Fluid domain

The governing equations of the advecting fluid flow are the continuity equation and the incompressible Navier–Stokes equations, respectively

$$\nabla \cdot \boldsymbol{u}^f = 0 \tag{1}$$

$$\partial_t \boldsymbol{u}^f + \boldsymbol{u}^f \cdot \nabla \boldsymbol{u}^f = -\nabla p^f + \nu \nabla^2 \boldsymbol{u}^f + \boldsymbol{g}^f, \tag{2}$$

where $\boldsymbol{u}^f(\boldsymbol{x}, t) = (u^f, v^f)$ is the velocity vector field, $p^f(\boldsymbol{x}, t)$ is the scalar pressure field, ν is the fluid kinematic viscosity, $\boldsymbol{x} = (x, y)$ is the spatial coordinates vector, t is time, $\boldsymbol{g}$ are the body forces, and the script f refers to variables in the Ω^f domain. The pressure-Poisson equation is solved with a predictor-corrector (projection) method which imposes the divergence-free condition on the velocity field. The no-slip boundary condition is enforced on the solid channel walls, i.e. $\boldsymbol{u}^f|_{y=0,h} = 0$. A periodic boundary condition is enforce on the x direction, i.e. $\boldsymbol{u}^f|_{x=0} = \boldsymbol{u}^f|_{x=5h}$ and $p^f|_{x=0} = p^f|_{x=5h}$. The planar Poiseuille flow solution is employed as initial condition for the velocity field in Ω^f, i.e. $\boldsymbol{u}_0^f = (u_0^f, 0)$ with

$$u_0^f = \frac{G}{2\mu} y(h - y), \tag{3}$$

where μ is the fluid dynamic viscosity, and G is the arbitrary constant pressure drop ($G = -\mathrm{d}P/\mathrm{d}x$) that acts as a body force and drives the flow in the streamwise periodic domain. i.e. $\boldsymbol{g}^f = (G, 0)$.

Porous domain

The Darcy's law can be used to describe fluid flow through a porous medium. For an isotropic porous material, the Darcy's law can be written as

$$\boldsymbol{u}^p = -\frac{k}{\varphi\mu}\nabla p^p, \tag{4}$$

where φ and k are the porosity and permeability of the porous medium, and the script p refers to variables in the Ω^p domain. The porous flow velocity $\boldsymbol{u}^p$ must also satisfy the divergence-free condition

$$\nabla \cdot \boldsymbol{u}^p = 0. \tag{5}$$

Taking the divergence of Eq. 4 and using Eq. 5, a Laplace equation is found describing the pressure field in the porous medium

$$\frac{k}{\varphi\mu}\nabla^2 p^p = 0. \tag{6}$$

Similarly, taking the curl of Eq. 4 yields the irrotationality of the Darcy velocity field $\nabla \times \boldsymbol{u}^p = 0$.

On the interface $\partial\Omega$ between Ω^f and Ω^p, we impose continuity of normal flux, continuity of pressure, and no-slip condition for the tangential velocity component, respectively

$$\boldsymbol{u}^f \cdot \boldsymbol{n} = \boldsymbol{u}^p \cdot \boldsymbol{n} \tag{7}$$

$$p^f = p^p \tag{8}$$

$$\boldsymbol{u}^f \cdot \boldsymbol{s} = \boldsymbol{u}^f - (\boldsymbol{u}^f \cdot \boldsymbol{n})\boldsymbol{n} = 0. \tag{9}$$

Rigid body motion

The transport of a porous particle is modelled using planar rigid body motion, hence no deformation of the particle is considered. The pressure and velocity on the surface $\partial\Omega$, respectively q and $\boldsymbol{v}$, advect the constant-mass (m) porous particle according to the law of conservation of linear momentum

$$\boldsymbol{F} := \int_{\partial\Omega} \left[-qI + \mu\left(\nabla\boldsymbol{v} + \nabla\boldsymbol{v}^\top\right)\right] \cdot \boldsymbol{n}\, \mathrm{d}\mathcal{S} \tag{10}$$

$$m\frac{\mathrm{d}\boldsymbol{v}}{\mathrm{d}t} = \boldsymbol{F}. \tag{11}$$

The centre of mass velocity ($\boldsymbol{v}_c$) and position ($\boldsymbol{y}_c$) of the particle are obtained by integrating Eq. 11 as follows

$$\boldsymbol{v}_c^{n+1} = \boldsymbol{v}_c^n + \frac{\delta t}{m}\boldsymbol{F}^n \tag{12}$$

$$\boldsymbol{y}_c^{n+1} = \boldsymbol{y}_c^n + \delta t\left(\boldsymbol{v}_c^n + \frac{\delta t}{2m}\boldsymbol{F}^n\right). \tag{13}$$

In addition to translation, angular motion is also considered. The angular position (θ) and the angular velocity ($\varpi = \dot{\theta}$) are computed from the conservation of angular momentum

$$I_c\frac{\mathrm{d}\varpi}{\mathrm{d}t} = T_z, \tag{14}$$

where Tz is the torque (in the z) axis defined as $T_z = \boldsymbol{r} \times \boldsymbol{F}$, $\boldsymbol{r} := \boldsymbol{y} - \boldsymbol{y}_c$ is the position vector from the centre of mass of the particle ($\boldsymbol{y}_c$) to its surface ($\partial\Omega$), and I_c is the $\boldsymbol{e}_z$ moment of inertia of the particle through its centre of mass. If particles are shaped like an ellipse, their moment of inertia would be given by $I_c = m(a^2+b^2)/4$, where a and b are the ellipse major and minor semi-axis. Similarly to Eq. 12 and Eq. 13, the integration of Eq. 14 yields the particle angular velocity and position, respectively

$$\varpi^{n+1} = \varpi^n + \frac{\delta t}{I_c} T_z^n \tag{15}$$

$$\theta^{n+1} = \theta^n + \delta t \left(\varpi^n + \frac{\delta t}{2 I_c} T_z^n \right). \tag{16}$$

Finally, the superposition of translation and rotation yields to the new position and velocity of the particle

$$\boldsymbol{y}^{n+1} = \boldsymbol{y}_c^{n+1} + \underline{\boldsymbol{R}}(\theta^{n+1}) \boldsymbol{y}^n \tag{17}$$

$$\boldsymbol{v}^{n+1} = \boldsymbol{v}_c^{n+1} + \varpi^{n+1} \boldsymbol{r}^{\perp}, \tag{18}$$

where the script $\perp$ denotes perpendicularity, and $\underline{\boldsymbol{R}}$ is the planar rotation matrix

$$\underline{\boldsymbol{R}}(\theta) = \begin{bmatrix} \cos\theta & -\sin\theta \\ \sin\theta & \cos\theta \end{bmatrix}. \tag{19}$$

Fluid-structure interaction

The coupling between the governing equations of fluid and porous regions is exemplified next using a free-moving porous piston in a 1-D domain. The flow starts at rest and the piston motion is driven by the background pressure gradient. Fig. 2 sketches the problem domain.

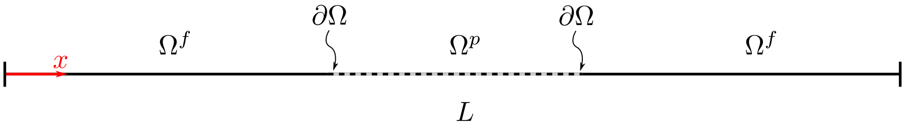

Figure 2: Sketch of the 1-D free-moving piston test case. See Fig. 1 for nomenclature.

The boundary data immersion method (BDIM) is employed to couple the fluid and porous governing equations. In short, BDIM combines different physics in a single meta-equation ($\mathcal{M}^\epsilon$) using a convolutional kernel which facilitates a smooth transition between the different domains. In this case, the fluid and the porous governing equations are, respectively,

$$\mathcal{F} := \partial_t u^f + u^f \partial_x u^f + \rho^{-1} \partial_x p^f - \nu \partial_{xx} u^f - f^f = 0, \tag{20}$$

$$\mathcal{P} := u^p + \beta \partial_x p^p = 0, \tag{21}$$

where $\beta = k/(\varphi\mu)$. The continuity equation is also enforced in both domains, $\partial_x u^f = \partial_x u^p = 0$, and this simplifies the fluid momentum equation to $\mathcal{F} := \partial_t u^f + \rho^{-1} \partial_x p^f - f^f = 0$.

The convolution kernel (K^ϵ) extends (e.g.) the porous subdomain (Ω^p) to the whole domain (Ω) as follows (can be analogously derived for the fluid subdomain equation)

$$\mathcal{P}^\epsilon(x) = \int_{\Omega^p} \mathcal{P}(x^p) K^\epsilon(x, x^p) \, \mathrm{d}x^p \approx \mathcal{P}(x) \int_{\Omega^p} K^\epsilon(x, x^p) \, \mathrm{d}x^p, \tag{22}$$

$$\mathcal{P}^\epsilon(x) \approx \mathcal{P}(x) \mu^p. \tag{23}$$

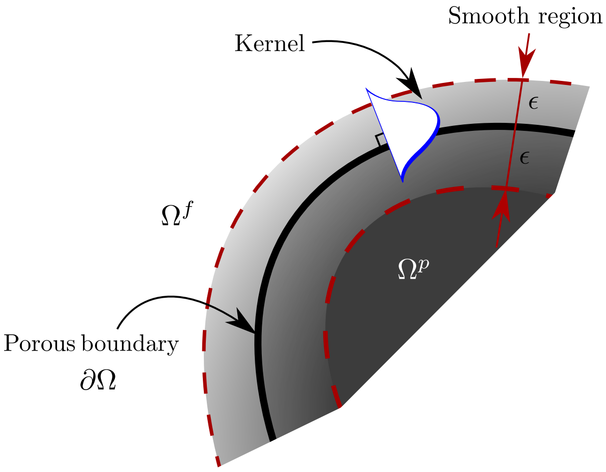

Figure 3: A convolution kernel with radius ϵ smooths the interface between fluid (Ω^f) and porous (Ω^p) subdomains.

The integrated kernel over the porous subdomain, μ^p, can take the approximated form

$$\mu^p(d) = \begin{cases} \frac{1}{2}[1+\sin(\frac{\pi}{2}\frac{d}{\epsilon})] & \text{for } |d| < \epsilon \\ 1 & \text{for } d < -\epsilon \\ 0 & \text{else,} \end{cases} \tag{24}$$

where d is a signed-distance function from a point x to the fluid-porous interface ($\partial\Omega$) and 2ϵ is the interface thickness (see Fig. 3). Also note that $\mu^f = 1 - \mu^p$. With this, the meta-equation combining both governing equations reads

$$\mathcal{M}^\epsilon := (1-\mu^p)\mathcal{F} + \mu^p\mathcal{P} = 0. \tag{25}$$

To numerically solve Eq. 25, the fluid governing equation $\mathcal{F}$ is integrated in time as

$$u^f_{n+1} - u^f_n = h_{\delta t}(u^f_n) - \partial p^f_{\delta t} + f^f_{\delta t}, \tag{26}$$

where the RHS terms are the time-integrated convection-diffusion term, pressure term, and body force term, respectively

$$h_{\delta t}(u^f_n) = \int_{t_n}^{t_n+\delta t} (-u^f\partial_x u^f + \nu\partial_{xx}u^f)\,\mathrm{d}t, \tag{27}$$

$$\partial p^f_{\delta t} = \int_{t_n}^{t_n+\delta t} \rho^{-1}\partial_x p^f\,\mathrm{d}t, \tag{28}$$

$$f^f_{\delta t} = \int_{t_n}^{t_n+\delta t} f^f\,\mathrm{d}t. \tag{29}$$

Using the expressions above, the meta-equation $\mathcal{M}^\epsilon$ can be written as

$$u^\epsilon_{n+1} = (1-\mu^p)(u^\epsilon_n + h^\epsilon_{\delta t} - \partial p^\epsilon_{\delta t} + f^\epsilon_{\delta t}) - \mu^p(\beta\partial_x p^\epsilon), \tag{30}$$

where u^ϵ_{n+1} is the next time step velocity field defined on the whole domain Ω.

The time integrals in Eqs. 27 to 29 can be evaluated using (e.g.) an Euler explicit forward time-integration scheme, and a projection method is used to enforce the divergence-free condition on the velocity field as follows

$$u^* = (1-\mu^p)(u^\epsilon_n + h^\epsilon_{\delta t} + f^\epsilon_{\delta t}), \tag{31}$$

$$\partial_x u^\epsilon_{n+1} = \partial_x u^* - \partial_x[(1-\mu^p)\delta t\rho^{-1}\partial_x p^\epsilon + \mu^p\beta\partial_x p^\epsilon] = 0, \tag{32}$$

$$u^\epsilon_{n+1} = u^* - [(1-\mu^p)\delta t\rho^{-1} + \mu^p_\epsilon\beta]\partial_x p^\epsilon. \tag{33}$$

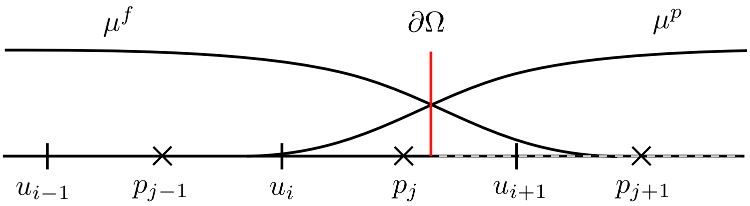

Figure 4: Staggered grid used in the finite volume method. The fluid and porous integrated kernels, respectively μ^f and μ^p, are also depicted.

Using a finite-volume method in a staggered grid (see Fig. 4) and considering the divergence theorem, Eq. 32 can be written as follows (now using subscripts for grid index instead of temporal index)

$$\frac{1}{\mathcal{V}_j}\int_{\mathcal{V}_j}\partial_x\left(\mu^f\delta t\rho^{-1}\partial_x p^\epsilon+\mu^p\beta\partial_x p^\epsilon\right)\mathrm{d}\mathcal{V}_j=\frac{1}{\mathcal{V}_j}\int_{\mathcal{V}_j}\partial_x u^*\,\mathrm{d}\mathcal{V}_j \tag{34}$$

$$\frac{1}{\delta x}\int_{\mathcal{S}_j}\left(\mu^f\delta t\rho^{-1}\partial_x p^\epsilon+\mu^p\beta\partial_x p^\epsilon\right)\cdot n\,\mathrm{d}\mathcal{S}_j=\frac{1}{\delta x}\int_{\mathcal{S}_j}u^*\cdot n\,\mathrm{d}\mathcal{S}_j, \tag{35}$$

where $\mu^f\partial_x p^\epsilon$ and $\mu^p\partial_x p^\epsilon$ must be first computed on the cell face of the pressure control volume defined as $\mathcal{V}_j=[x_{j-1/2},x_{j+1/2}]=[x_i,x_{i+1}]$, noting $\delta x=x_{i+1}-x_i$. The following central-difference discretisation is considered to approximate the face values of the pressure gradient

$$\mu^f\partial_x p^\epsilon|_{j+1/2}\approx\mu^f_{j+1/2}\,\partial_x p^\epsilon|_{j+1/2}=\mu^f_{i+1}\frac{p^\epsilon_{j+1}-p^\epsilon_j}{\delta x}, \tag{36}$$

$$\mu^f\partial_x p^\epsilon|_{j-1/2}\approx\mu^f_{j-1/2}\,\partial_x p^\epsilon|_{j-1/2}=\mu^f_{i}\frac{p^\epsilon_{j}-p^\epsilon_{j-1}}{\delta x}. \tag{37}$$

With this, Eq. 35 can be computed as

$$\frac{1}{\delta x}\left[\left(\mu^f\delta t\rho^{-1}\partial_x p^\epsilon+\mu^p\beta\partial_x p^\epsilon\right)|_{j+1/2}-\left(\mu^f\delta t\rho^{-1}\partial_x p^\epsilon+\mu^p\beta\partial_x p^\epsilon\right)|_{j-1/2}\right]=\frac{u^*_{i+1}-u^*_i}{\delta x} \tag{38}$$

$$\frac{1}{\delta x}\left[\left(\mu^f_{i+1}\delta t\rho^{-1}+\mu^p_{i+1}\beta\right)\frac{p^\epsilon_{j+1}-p^\epsilon_j}{\delta x}-\left(\mu^f_i\delta t\rho^{-1}+\mu^p_i\beta\right)\frac{p^\epsilon_j-p^\epsilon_{j-1}}{\delta x}\right]=\frac{u^*_{i+1}-u^*_i}{\delta x} \tag{39}$$

$$\frac{\alpha_{i+1}p^\epsilon_{j+1}-\left(\alpha_{i+1}+\alpha_i\right)p^\epsilon_j+\alpha_i p^\epsilon_{j-1}}{\delta x^2}=\phi_j, \tag{40}$$

where $\alpha_i=\mu^f_i\delta t\rho^{-1}+\mu^p_i\beta$ and $\phi_j=\left(u^*_{i+1}-u^*_i\right)/\delta x$. Eq. 40 can be posed as

$$Ap^\epsilon=\phi \tag{41}$$

and α_i are the coefficients used to construct the pressure matrix A,

$$A_{ij}=\frac{1}{\delta x^2}\begin{bmatrix}-(\alpha_1+\alpha_2) & \alpha_2 & 0 & \dots & 0 & 0 & \alpha_1\\ \alpha_2 & -(\alpha_2+\alpha_3) & \alpha_3 & 0 & \dots & 0 & 0\\ 0 & \alpha_3 & -(\alpha_3+\alpha_4) & \alpha_4 & 0 & \dots & 0\\ \vdots & \ddots & \ddots & \ddots & \ddots & \ddots & \vdots\\ 0 & \cdots & 0 & \alpha_{N-2} & -(\alpha_{N-2}+\alpha_{N-1}) & \alpha_{N-1} & 0\\ 0 & 0 & \cdots & 0 & \alpha_{N-1} & -(\alpha_{N-1}+\alpha_N) & \alpha_N\\ \alpha_1 & 0 & 0 & \cdots & 0 & \alpha_N & -(\alpha_N+\alpha_1)\end{bmatrix} \tag{42}$$

where periodic boundary conditions are used: $A_{1N}=\alpha_1$ and $A_{N1}=\alpha_1$. A conjugate gradient method is used to solve Eq. 40 yielding p^ϵ_j in the 1-D grid discretised with N finite volumes.

Next, results are presented for both fluid-solid (FS) and fluid-porous (FP) domain configurations. The following parameters are selected: $L=[-1,1]$, $t=[0,2]$, $\nu=0.004$ ($Re=UL/\nu=500$), $\rho=1$, $g^f=-\partial_x P=1$, $m=0.1$ (same for solid and porous pistons), $\varphi=0.5$, $k=10^{-4}$, $\beta=k/(\varphi\nu\rho)=0.05$.

Fig. 5 displays the position of the piston for both FS and FP configurations together with the pressure and velocity solution on the whole domain at $t = 1.5$ and $t = 2$. It can be observed that the FP configuration achieves a lower fluid velocity (u^ϵ) which eventually becomes constant. This is clearly appreciated in Fig. 6, where the temporal evolution of the piston position and velocity is presented for both cases. On the other hand, the velocity of the piston itself becomes higher than the solid case at $t = 1.4$. The following observations are noted: a) the velocity of the porous piston does not match the velocity of the fluid, contrary to the solid piston where piston velocity and fluid velocity match because of the no-slip velocity condition. b) since the fluid velocity of the FP case does not match the velocity of the piston, the fluid velocity can reach a terminal velocity different to the (always) accelerating piston velocity (driven by the forced background pressure gradient force).

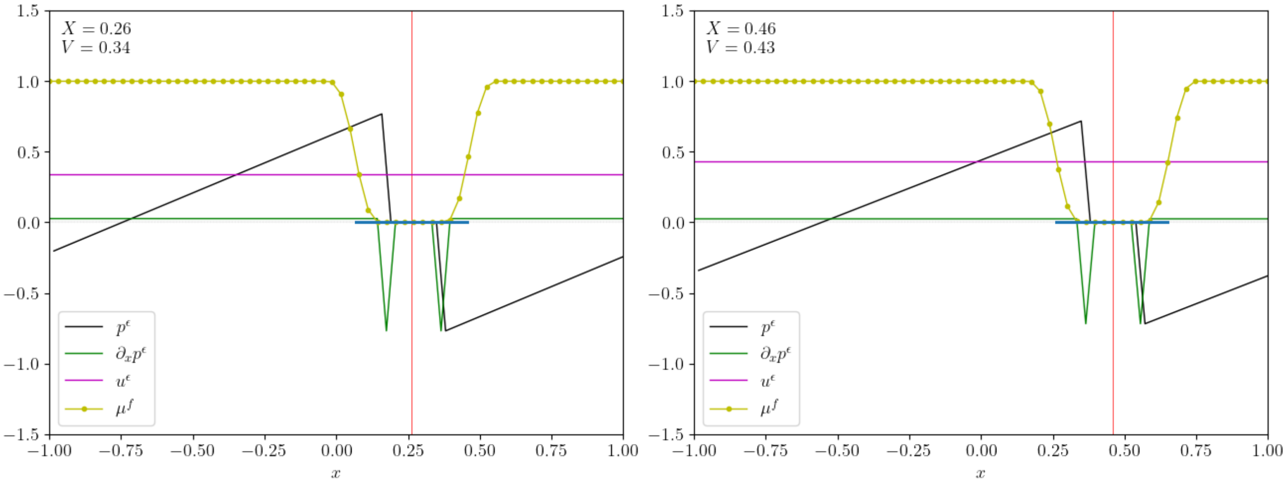

(a) FS solution at $t = 1.5$.

(b) FS solution at $t = 2.0$.

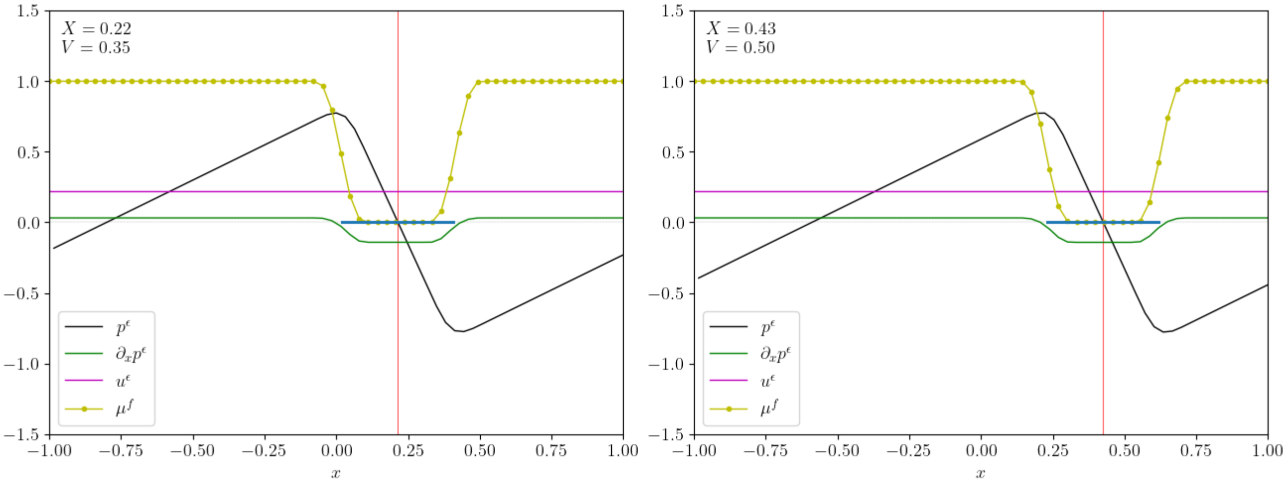

(c) FP solution at $t = 1.5$.

(d) FP solution at $t = 2.0$.

Figure 5: Solution of the 1-D free-moving piston for the fluid-solid (top) and fluid-porous (bottom) configurations at $t = 1.5$ (left) and $t = 2.0$ (right). The piston position (X) and velocity (V) are indicated at the top left corner. The piston region is defined by the blue horizontal line, and the vertical red line indicates its centre position X. The fluid velocity u^ϵ and pressure p^ϵ are depicted in purple and dashed black lines, respectively.

With regard to the solution of the porous piston case, a linear pressure distribution can be observed within the porous region. In turn, there is a constant velocity distribution within the porous region, satisfying Eq. 4. Additionally, the normal flow velocity continuity BC (Eq. 7) and the pressure continuity BC (Eq. 8) across the fluid-porous interface are being satisfied as well. However, the no-tangential flow velocity BC (Eq. 9) cannot be tested in the 1-D problem, and a 2-D system is required to assess the correct implementation of this condition with the current methodology.

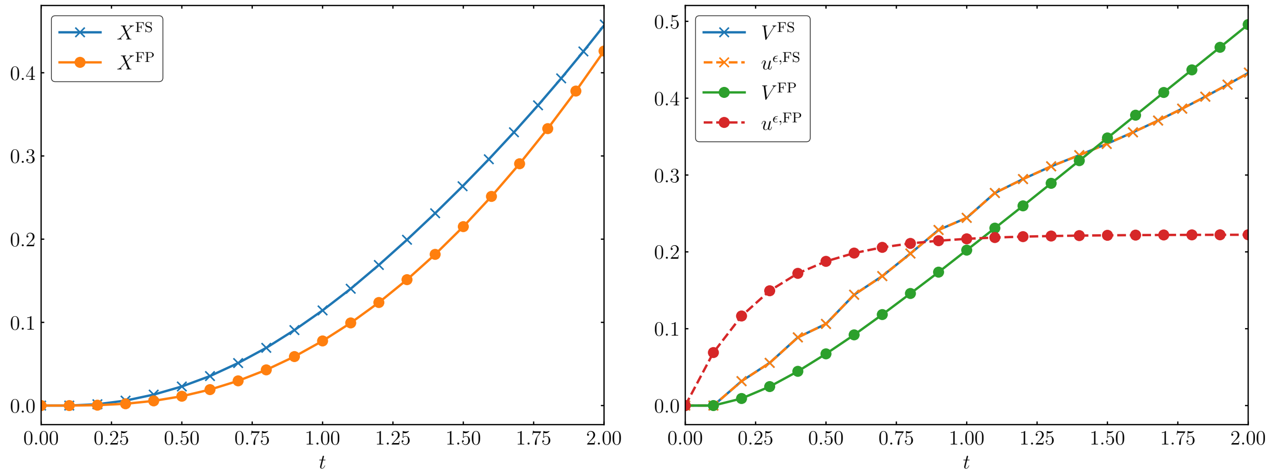

Figure 6: Temporal evolution of piston position (left) and velocity (right) of both FS and FP cases.

Last, the porous region effect on the flow solution is assessed by modifying the piston porosity from $\varphi = 0.5$ to $\varphi = 0.1$, resulting in $\beta = 0.25$, i.e. an even more "porous-like" region than the previous set-up. The flow solution of the $\beta = 0.25$ porous case is depicted in Fig. 7. Compared to the $\beta = 0.05$ case, the piston does not travel as far and achieves a lower velocity. Yet, the fluid reaches a higher velocity, and this can be better appreciated in Fig. 8, where the temporal evolution of the solution is shown and compared to the $\beta = 0.05$ case. With this, it can be concluded that the higher the porosity effect, the less energy can be transfered from fluid to structure hence the structure is less responsive to the fluid impulse force. On the other hand, it has been observed that the fluid velocity has been both lower and higher for the $\beta = 0.05$ and $\beta = 0.25$ cases, respectively, compared to the solid piston case. Therefore, it is not clear yet what is the actual effect of having a porous region on the fluid region velocity. A more comprehensive sweep of β is required to in this regard.

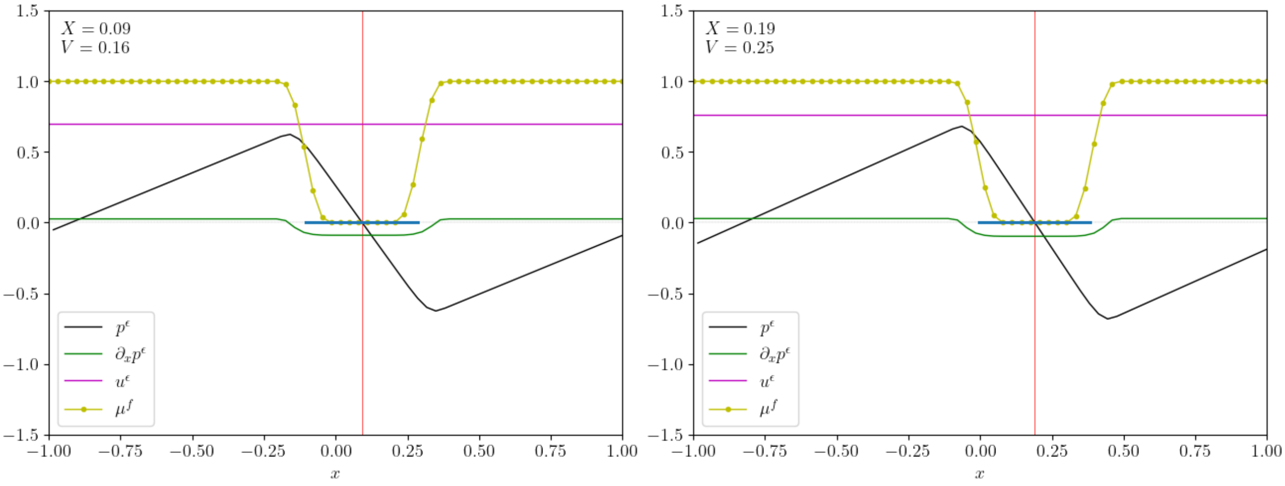

(a) FP solution at $t = 1.5$.

(b) FP solution at $t = 2.0$.

Figure 7: Solution of the 1-D free-moving piston for the $\beta = 0.25$ fluid-porous case at $t = 1.5$ (left) and $t = 2.0$ (right). See Fig. 5 for figure description.

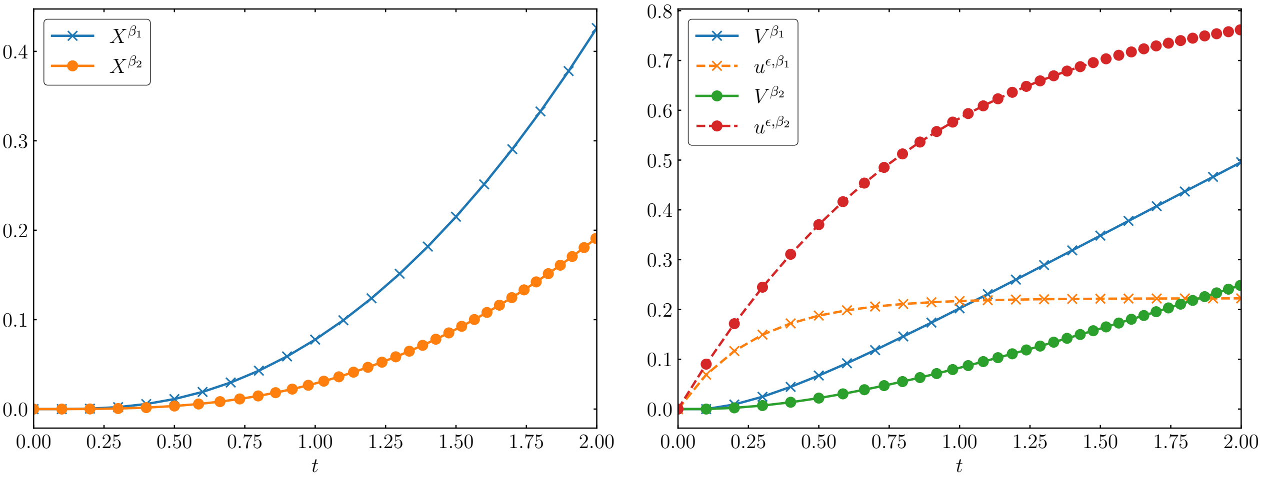

Figure 8: Temporal evolution of piston position (left) and velocity (right) of both porous cases where $\beta_1 = 0.05$ and $\beta_2 = 0.25$.